Draft version March 10, 2023
Typeset using LaTeX default style in AASTeX631

Comprehensive radiative MHD simulations of flares above collisional polarity inversion lines

Matthias Rempel,[1] Georgios Chintzoglou,[2] Mark C. M. Cheung,[3] Yuhong Fan,[1] and Lucia Kleint[4]

[1] *High Altitude Observatory, National Center for Atmospheric Research, P.O. Box 3000, Boulder, CO 80307, USA*
[2] *Lockheed Martin Solar and Astrophysics Laboratory, Palo Alto, CA, USA*
[3] *CSIRO, Space & Astronomy, PO Box 76, Epping, NSW 1710, Australia*
[4] *Astronomical Institute of the University of Bern, Sidlerstrasse 5, 3012 Bern, Switzerland*

ABSTRACT

We present a new simulation setup using the MURaM radiative MHD code that allows to study the formation of collisional polarity inversion lines (cPILs) in the photosphere and the coronal response including flares. In the setup we start with a bipolar sunspot configuration and set the spots on collision course by imposing the appropriate velocity field at the footpoints in the subphotospheric boundary. We vary parameters such as the initial spot separation, collision speed and collision distance. While all setups lead to the formation of a sigmoid structure, only the cases with a close passing of the spots cause flares and mass eruptions. The energy release is in the $1 - 2 \times 10^{31}$ ergs range, putting the simulated flares into the upper C to lower M-class range. While the case with the more distant passing of the spots does not lead to a flare, the corona is nonetheless substantially heated, suggesting non-eruptive energy release mechanisms. We focus our discussion on two setups that differ in spot coherence and resulting cPIL length. We find different timings in the transition from a sheared magnetic arcade (SMA) to magnetic flux rope (MFR): the setup with a short cPIL produces a MFR during the eruption, while the MFR is pre-existing in the setup with a longer cPIL. While both result in flares of comparable strength, only the setup with pre-existing MFR produces a CME.

Keywords: Sun: activity, Sun: magnetic fields, Sun: flares, Sun: coronal mass ejections (CMEs), methods: numerical

1. INTRODUCTION

Based on observations there is solid statistical evidence that active regions (ARs) with complex polarity inversion lines are very flare- and CME-productive (Schrijver 2007). Statistical flare forecasting approaches such as Gallagher et al. (2002); Cui et al. (2006, 2007); Barnes et al. (2007); Georgoulis & Rust (2007) rely on various measures of AR complexity (such as PIL length, field gradients across PIL, vertical current, shear angle of magnetic field) and generally find a higher likelihood for flares in more complex ARs. The most flare productive ARs are often associated with δ-spots (classification introduced by Künzel 1960), which are characterized by umbrae of opposite polarities sharing a penumbra, and a significant effort in modeling has focused on understanding how they form and how they energize the corona and lead to strong flares. While Linton et al. (1998, 1999); Takasao et al. (2015) studied the formation of δ-spots through the emergence of twisted, kink-unstable flux tubes, Toriumi et al. (2014); Fang & Fan (2015) showed that flows during flux emergence, resulting from mass drainage, can pin down sections of a rising flux-bundle and lead to more complex magnetic field distributions in the photosphere. A more systematic study by Toriumi & Takasao (2017) investigated four possible scenarios (spot-spot interaction from kink-unstable flux tube, spot-satellite interaction, quadrupolar setups from convective (or buoyant) down pinning of a rising flux bundle, and the interaction of two rising flux bundles). The latter scenario was used by Toriumi et al. (2014) to simulate the formation of NOAA AR11158, a very flare-productive AR that appeared in February 2011. While their setup produced non-potential shear, the resulting mostly interlocked polarities did not reproduce the phenomenology of AR11158 as described in

rempel@ucar.edu

Chintzoglou et al. (2019), which showed the colliding polarities to slide past each other. Chintzoglou et al. (2019) identified a process in which typically two AR-forming flux bundles emerge in close proximity (either simultaneously or after each other), leading to a quadrupolar magnetic field configuration in which the non-conjugate polarities (i.e. polarities from different bipolar groups) interact with each other through a process of collisional shearing.

While the above summarized MHD simulations focused on the formation of δ-spots in the photosphere, they did not study how the δ-spots formation influences the buildup and release of free energy in the overlying corona leading eventually to energetic flares. This was studied by Chintzoglou et al. (2019) with the help of magneto-frictional modeling, showing how the the delta-spot lead to the formation of a pre-eruptive MFR.

One critical aspect of the coronal magnetic field evolution concerns the question of how and when a magnetic flux rope (MFR) forms during the energy buildup and eruption process. It was proposed by Antiochos et al. (1999); Lynch et al. (2008) that MFRs form "on-the-fly" during the eruption process through resistive processes at the reconnection site. The alternative scenario is a pre-existing MFR that formed during the energy buildup phase and destabilizes due to ideal MHD instabilities (e.g., Kliem & Török 2006). These two scenarios are not mutually exclusive, since a pre-existing MFR can be enhanced during the eruption, and the pre-eruption configuration can exist in a hybrid state with a smooth transition from a sheared magnetic arcade (SMA) to a MFR (Patsourakos et al. 2020).

The main focus of this paper is studying the evolution of the coronal magnetic field during the process of collisional shearing from the early stages of energy buildup to eruption. Central to this process is the formation of a collisional polarity inversion line (cPIL). A cPIL considers that strong magnetic flux elements ($|B_z| \geq 100\,\mathrm{G}$) are clashing at a distance $\leq 1.8\,\mathrm{Mm}$ along the PIL (Chintzoglou et al. 2019), and similar studies by Liu et al. (2019, 2021); Wang et al. (2022). Most ARs with collisional shearing include at least two interacting bipolar groups (i.e. a quadrupolar setup), and the cPIL forms in-between the non-conjugated polarities (i.e. polarities from different bipolar groups). We simplify our setup to only include the two (non-conjugated) interacting polarities, essentially by disregarding the non-colliding conjugated polarities. We emphasize that the evolution presented here shall be understood by always keeping the two omitted non-colliding polarities in mind, according to the collisional shearing scenario. In fact, rapidly converging proper motions are not seen in simple emerging bipoles (instead, we see diverging proper motions during the emergence phase of simple bipoles; see Figure 1, in Chintzoglou et al. (2019)). This is also not to be confused with the van Ballegooijen & Martens (1989) scenario that considers a decaying conjugate bipole, where cancellation happens in the internal neutral line as a result of flux decay. In our setup, the high speed of the moving polarities is inspired by the rapid relative motions driven during the emergence phase of separate bipoles; collision happens in the external PIL of such separate bipoles composing multi-polar ARs (see Figures 12 and 15 in Chintzoglou et al. (2019)). Furthermore, this setup removes complexities originating from flux emergence, as we simply translate the magnetic polarities, while still allowing for cancellation in the photosphere.

We describe the model setup in section 2, present the results in section 3 and discuss future observations that could directly differentiate between SMAs and MFRs through magnetic observations in section 4. We summarize our conclusions in section 5.

2. SIMULATION SETUP

For the simulations presented here we use the Coronal extension of the MURaM code (Rempel 2017) that has been successfully used for solar flares simulations as reported in Cheung et al. (2019). We use a domain with the extents of $98.304 \times 49.152 \times 73.728$ Mm^3 with a grid cell size of $192 \times 192 \times 64$ km^3. The location of the photosphere is about 3.4 Mm above the bottom boundary condition. The domain is periodic in the horizontal directions. The top boundary is open for vertical flows and the magnetic field is matched to a potential field extrapolation. Outside regions of strong magnetic field the bottom boundary condition is open as described in Rempel (2014). The initial magnetic field configuration consists a pair of spots with 3×10^{31} Mx flux at a separation of 25 Mm. This setup was evolved for several hours until the corona reached a relaxed state as described in Rempel (2017). At the footpoints of the sunspots we impose within a circle $\sqrt{(x - x_c(t))^2 + (y - y_c(t))^2} < R = 4\,\mathrm{Mm}$ (we follow here the convention that the indices -2 and -1 correspond to the boundary cells, whereas the lowermost domain cells are 0 and 1):

$$\mathbf{M}_{-1} = \mathbf{M}_0\, a_M + \varrho_{-1}\mathbf{v}_{\mathrm{BND}}\,(1 - a_M)$$
$$\mathbf{M}_{-2} = \mathbf{M}_1\, a_M + \varrho_{-2}\mathbf{v}_{\mathrm{BND}}\,(1 - a_M) \quad (1)$$
$$\mathbf{B}_{-1} = \mathbf{B}_0\, a_B$$
$$\mathbf{B}_{-2} = \mathbf{B}_0\, a_B \quad (2)$$

Setup	v_x^0 [m/s]	v_y^0 [m/s]	ε_h	Collision speed [m/s]
A	-954	300	1.2	1000
B	-954	300	1	1000
C	-917	400	1.2	1000
D	-866	500	1.2	1000
E	-458	200	1.2	500

Table 1. Parameters for boundary driving used in the simulations. Runs A-D have a sunspot moving with 1000 m/s, run E with 500 m/s. Run B uses a parameter of $\varepsilon_h = 1$, which leads to a dispersal of the moving sunspots. In all other runs using $\varepsilon_h = 1.2$ the moving sunspot remains coherent throughout the duration of the simulations. The sequence of run (A,B), C and D leads to increasing collision distance, while runs C and E have similar collision distance but different collision speeds.

$$\begin{aligned} p_{-1} &= \bar{p}_0\, a_p + p'_0 \\ p_{-2} &= \bar{p}_0\, a_p^2 + p'_1 \end{aligned} \tag{3}$$

Here $\mathbf{M}$ and $\mathbf{B}$ are the vectors of mass flux and magnetic field, p and ϱ are gas pressure and density, $\bar{p}$ denotes the horizontally averaged pressure and p' the pressure perturbation. The coefficients a_v, a_B, a_p are given by

$$a_M = 0.8, \qquad a_B = |\mathbf{B}_0|/\max(0.8|\mathbf{B}_0|, |\mathbf{B}_1|), \qquad a_p = \bar{p}_0/\bar{p}_1 \tag{4}$$

and the imposed boundary velocity is related to the motion of the footpoint (x_c, y_c) through:

$$\mathbf{v}_{\mathrm{BND}} = (\varepsilon_h\, \dot{x}_c, \varepsilon_h\, \dot{y}_c, 0) \tag{5}$$

The parameter ε_h allows us to impose a footpoint velocity that differs slightly from $(\dot{x}_c, \dot{y}_c)$, which impacts the coherence of the footpoint. A choice of $\varepsilon_h < 1$ leads to steady flux loss, while $\varepsilon_h > 1$ minimizes flux loss by pushing the flux within the moving footpoint towards the leading edge with respect to the flow direction . In the equation for the mass flux boundary Eq. (1) a_M is a nudging parameter that pushes the velocity field in the boundary cells towards the imposed velocity $\mathbf{v}_{\mathrm{BND}}$, while the choice of $a_M = 0.8$ does lead to tight coupling, it minimizes artifacts from just imposing the velocity directly. The magnetic field Eq. (2) is extrapolated into the boundary cells using the gradient of the magnetic field strength present in the lowermost domain cells, given by a_B. The formulation of a_B from Eq. (4) prevents extreme values that would lead to numerical instability. The pressure boundary condition corresponds to an extrapolation of the mean stratification and a symmetric boundary for pressure fluctuations.

For the simulations presented here we held the left sunspot in place, i.e. $\mathbf{v}_{\mathrm{BND}} = 0$ and $(x_c, y_c) = (36.864\,\mathrm{Mm}, 24.576\,\mathrm{Mm})$, while we move the right sunspot according to the parameters as given in table 1 starting from the position$(x_c, y_c) = (61.44\,\mathrm{Mm}, 24.576\,\mathrm{Mm})$. For $t < t_{\mathrm{acc}}$ we increase the footpoint velocity linearly from 0 to $(\dot{x}_c, \dot{y}_c) = (v_x^0, v_y^0)$, for $t \geq t_{\mathrm{acc}}$ the velocity remains constant. In all simulations we use $t_{\mathrm{acc}} = 10^4$ s.

3. RESULTS

3.1. *General properties and energetics*

Figure 1 shows the initial photospheric magnetogram in panel a) and in panels b)-f) the magnetograms corresponding to the setups A-E at a time of 10 hours after the start of the simulations, close to the time of closest encounter and largest buildup of free energy in the domain. In this paper we will focus specifically on the setups A and B shown in panels b) and c). These setups have a similar collision speed and angle and only differ in the coherence of the moving positive polarity sunspot. At the time of collision the sunspot in setup B is dispersed over a length of more than 20 Mm, leading to a longer cPIL. While both simulations, as discussed in detail below, do have a flare of comparable strength there are distinct differences in the pre-eruption magnetic field configuration. In panels b) and c) we highlight with a vertical red line the position of cross-sections we discuss further in Figures 9 and 10

Figure 2 a) shows the buildup and release of free energy integrated over the volume starting with the average height of the $\tau = 1$ level in the photosphere. As reference magnetic field we use here the horizontally periodic potential field that is computed from the photospheric magnetogram. All cases reach free energies in the range of $3 - 6 \times 10^{31}$ ergs. For the coherent spot setups (A,) (C), (D) the peak free energy is found shortly after the closest encounter of the spots around $t = 9$ hours, for setup (E) with half the collision speed around $t = 17$ hours. The significantly lower

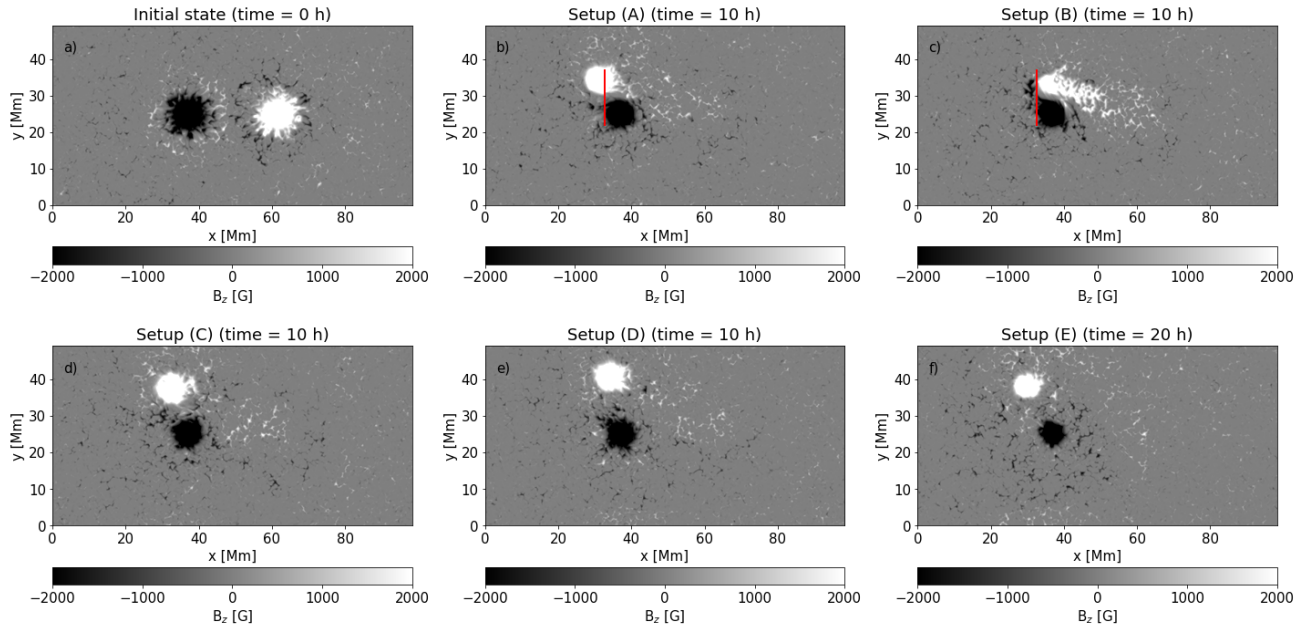

Figure 1. Photospheric magnetograms ($\tau = 0.1$). a) Initial state (identical for all setups); b-f) configuration found in setups (A)-(E) 10 hours after initiating the spot collision through velocity driving at the bottom boundary. Setups (A) and (B) differ in terms of coherence of the moving spot and will be analyzed in further detail later. The red vertical line indicates the position of vertical cross-sections presented in Figures 9 and 10.

energy release in setup (E) in comparison to setup (C) is likely due to 2 reasons: (1) the slower collisional speed allows for more coronal energy loss due to numerical resistivity during the buildup phase; (2) both polarities do show a continuous decay in the photosphere. The longer time to collision leads to spots with less flux and a larger effective separation during collision (which can be seen in Figure 1). In the case of the dispersing spot the free energy buildup is delayed by about 3 hours compared to setups (A), (C), and (D). Comparing setups (A) and (B) we find a comparable energy release of 2.5×10^{31} ergs during the flare, although setup (A) reaches with about 6.5×10^{31} ergs a higher value of free energy than setup (B) with about 5.2×10^{31} ergs, which makes these flares rather efficient in terms of releasing $40 - 50\%$ of the free energy. Setups (C) and (E) release energy in 2 smaller flares, setup (D) leads to a continuous energy release through multiple small-scale reconnection events. Figure 2, panels b)-e) show for each setup the height distribution of free magnetic energy as function of time, overlayed are the height contours under which 25/50/75% of the free energy are stored in each case. In all cases 50% of the free energy is stored below a height of 5 Mm at the time when flares occur.

Figure 3 shows a simulation snapshot from setup (B) at a time of 2.5 seconds before the flare. We show the photospheric magnetic field and synthetic AIA emission from 3 different view points. Specific to setup (B) is the formation of a filament channel that holds cool material and is visible in AIA 304 Å and 171 Å. We provide the full time evolution for all setups as movies in the online material.

Figure 4 shows the synthetic GOES-15 X-ray flux computed from the full simulation domain for the setups (A)-(E). Setups (A) leads to a C9 flare followed by a weaker secondary C4 flare at $t = 13.4$ hours, Setup (B) leads to a single M1 flare whereas setup (C) has a combination of C1 and a later C7 flare. Setups (D) and (E) reach C1 level, in the case of (D) without a distinct flare. The strong flares in setups (A) and (B) show a distinct double peak: a sharp peak at the end of impulsive phase and a more broad peak 20-30 minutes later. To our knowledge this has not been observed in real data, but, as we describe below, this behavior is similar to what is seen in late-phase EUV flares (Woods et al. 2011).

We further investigate the origin of the two GOES-15 emission peaks in Figure 5 where we show in panels a) - e) a map of the synthetic GOES flux together with the electron energy flux about 1 Mm above the average $\tau = 1$ level, which indicates the position of the flare ribbons. The electron energy flux is given by Spitzer conductivity that is limited during flare conditions by the free-streaming flux according to Fisher et al. (1985). The zero point in time corresponds to the peak on GOES X-ray flux as shown in panel e). 40.5 seconds before the flare peak (panel a) the

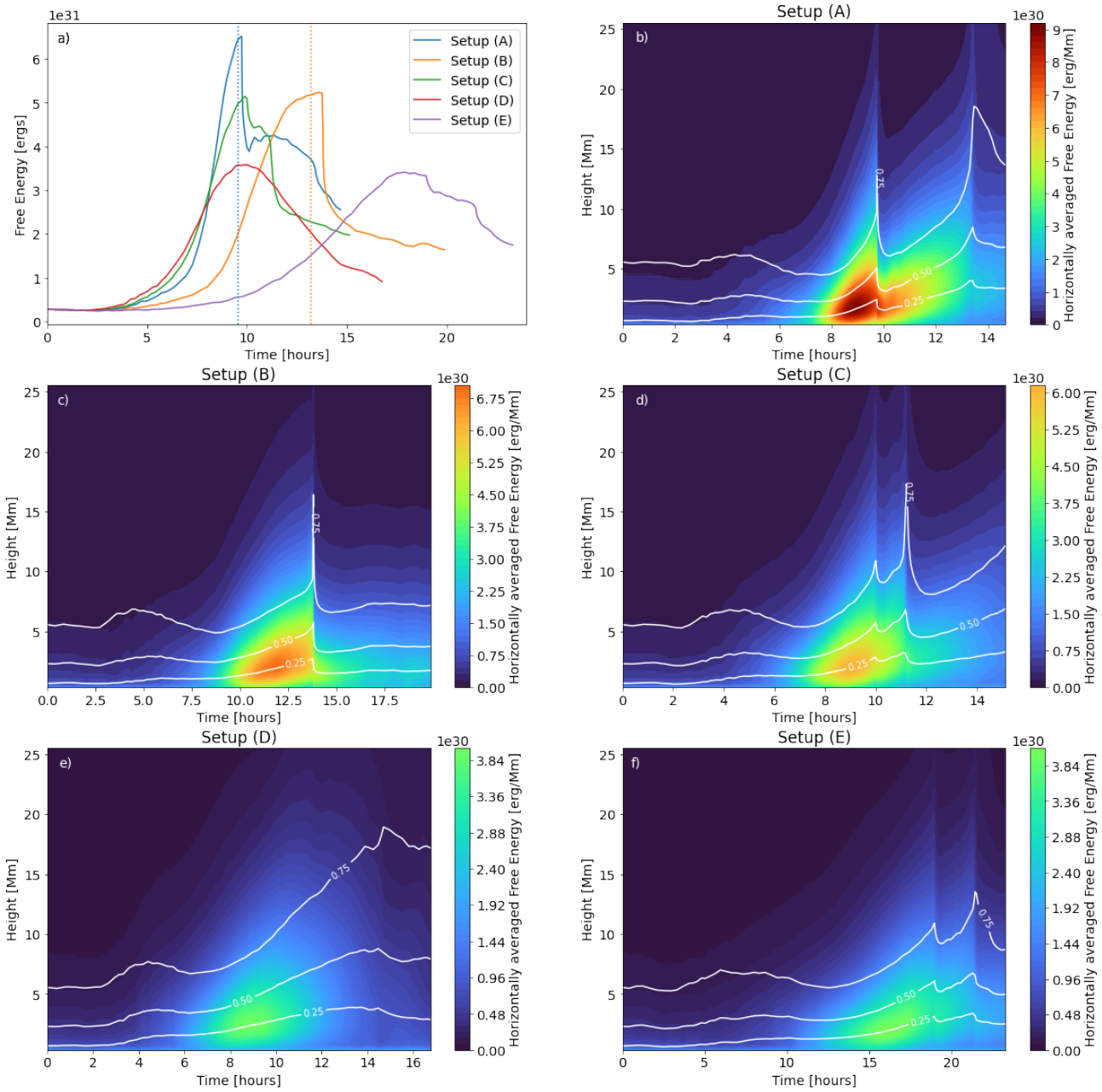

Figure 2. Buildup of free magnetic energy in Setups A-E. Panel a) shows the time evolution of free magnetic energy integrated over the coronal volume of the simulation domain. Panels b-f) show the time evolution of the horizontally averaged free magnetic energy for the individual cases. Here white contour lines indicate the height levels beneath which 25/50/75% of the free magnetic energy is stored. The vertical dotted lines in panel a) indicate the times for which we show the pre-eruption magnetic field configuration in Figure 8.

GOES-flux shows a sigmoid with enhancements of electron energy flux reaching 10^{10} ergs cm^{-1} s^{-1} in close proximity (onset of reconnection). During flare peak (panel b) the GOES flux highlights the hot post-flare loops, the electron energy flux reaches peak values of more than 10^{12} ergs cm^{-1} s^{-1} in small areas. 42.1 seconds after the flare (panel c) the post flare loops and flare ribbons start fading, while diffuse X-ray emission outside the central region of the flare starts to increase and to dominate about 313.3 seconds after the flare (panel d). The secondary peak is found about 25 minutes after the flare and is dominated by diffuse emission from most of the simulation volume (panel e).

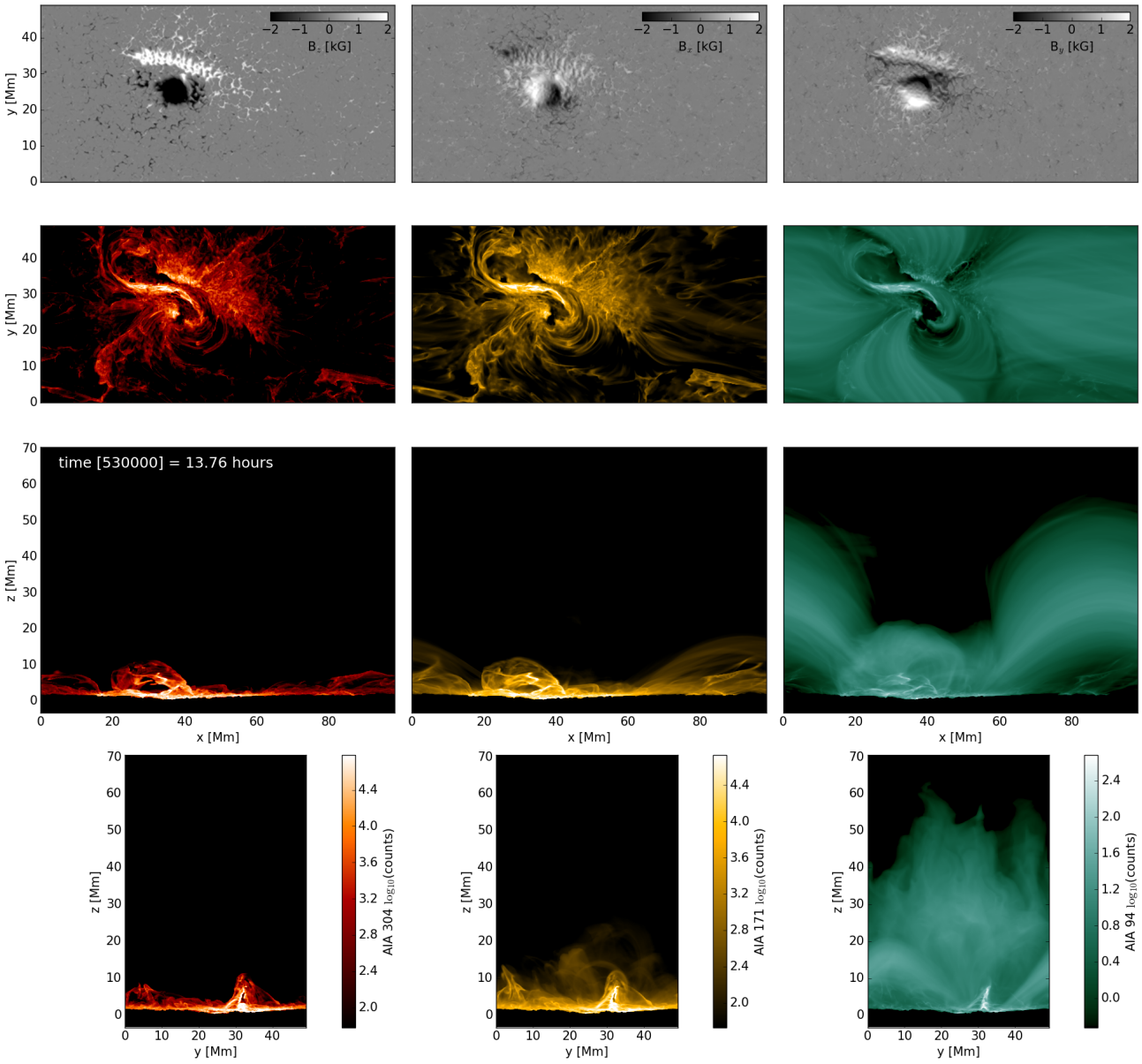

Figure 3. Photospheric and coronal appearance for setup (B). Top: Magnetic field in photosphere extracted on the $\tau_c = 0.1$ level. Bottom panels: synthetic AIA emission in the 304 Å, 171 Å and 94 Å channels computed for the three grid-aligned view direction as indicated by the axis labels. The snapshot corresponds to a time about 2.5 seconds before the flare peak as defined by the GOES X-ray flux. The side views show in AIA 304 Å and 171 Å a prominence that will erupt during the flare. An animation of this figure is provided with the online material.

The high electron energy fluxes found in this simulation are a consequence of energy release in a rather small volume. As discussed above, about 2.5×10^{31} ergs are released, most of that in heights of less than 5 Mm. We find reconnection outflows of up to 10,000 km s^{-1}, leading to peak plasma energy densities of about 0.5 MeV per particle (which would correspond to more than a billion K if interpreted as a thermal plasma). Our single fluid MHD approach cannot properly treat the exact partition of released energy between electrons and protons and expected deviations from Maxwellian distributions. However, a high energy density is in this setup unavoidable on the basis of energy conservation MHD is built upon. The secondary peak in the GOES-15 X-ray flux is consequence of this very hot plasma cooling down and passing through the GOES-15 response about 25 minutes after the flare. This becomes more evident from Figure 6, where we show in addition the shorter wavelength GOES-15 channel as well as simulated AIA 131 Å, 94 Å, 211 Å, 193 Å and 171 Å. The secondary peak appears first in the $0.5 - 4$ Å GOES-15 channel followed

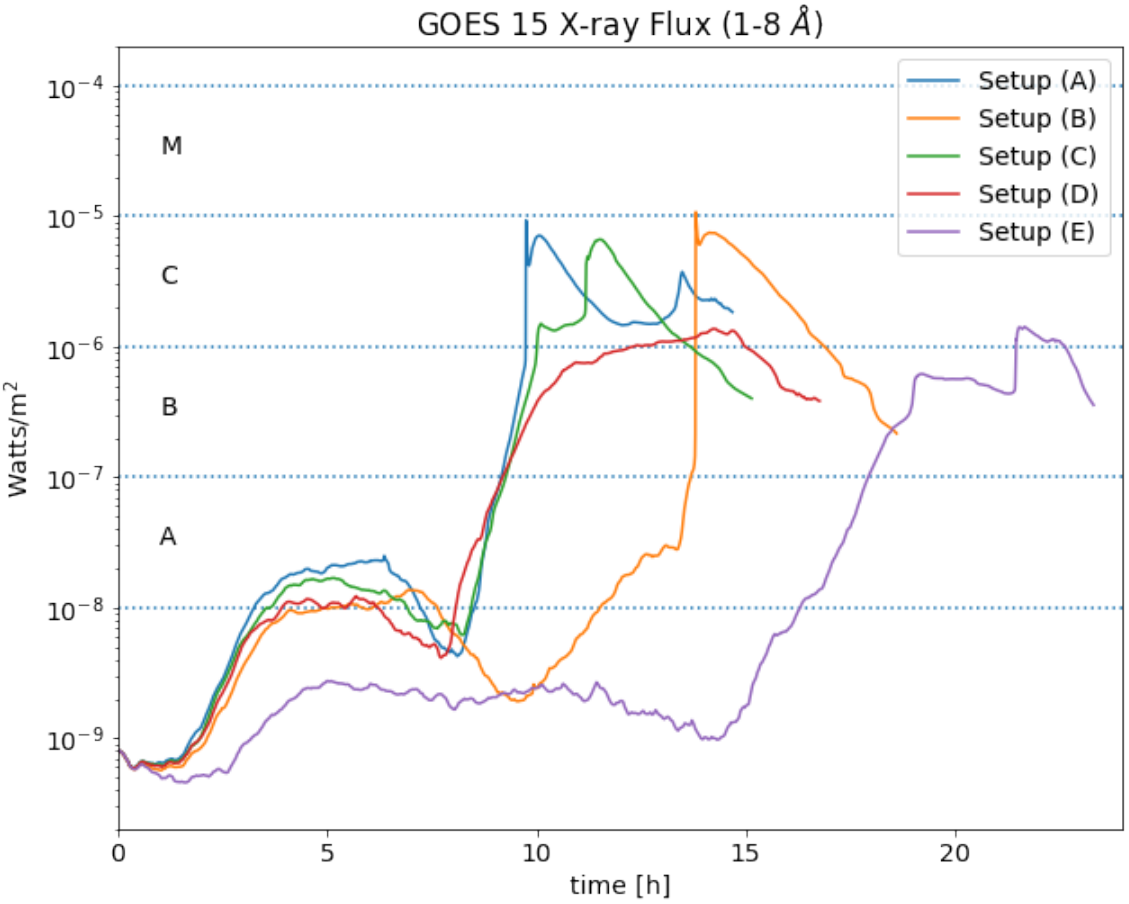

Figure 4. Synthetic GOES-15 X-ray flux computed for setups A-E. The two strongest flares found in setups A and B reach a strength of M1.

by the $1-8$ Å channel. About one hour after the flare peak we see a secondary peak in AIA 131 Å (this pass band has contributions around logT$\sim$ 5.7 and 7), followed by the secondary AIA 94 Å peak about 2 hours later. The pass bands of AIA 211 Å, 193 Å and 171 Å show a secondary peak about $4-5$ hours after the flare. Note that there is a tertiary peak of AIA 131 Å at around 5 hours, which results from the logT$\sim$ 5.7 contribution to this passband. This simulated flare is possibly an example for a late-phase EUV flare as described in Woods et al. (2011). In this type of flares a secondary peak in EUV emission originating not from the vicinity of the flare site is found minutes to hours after the flare.

3.2. *Evolution of magnetic field topology*

Figure 7 shows the pre-eruption magnetic field structure for setup (A) and (B) in panels a) and b), respectively. The presented snapshots correspond to the times indicated in Figure 2a) by vertical dotted lines. We show in Figure 7 magnetic field lines that are color coded by their twist number, i.e. the quantity:

$$T = \frac{1}{4\,\pi}\int \frac{(\nabla \times \mathbf{B})\cdot \mathbf{B}}{|\mathbf{B}|^2}\mathrm{d}s \tag{6}$$

computed above the photospheric average $\tau = 1$ level as indicated by the magnetogram. We only show field lines that have twist numbers above 1.2. While both setups do host strongly twisted field lines prior to the eruption, only setup (B) has a MFR with dipped field lines that can support a pre-eruption filament. While the magnetic field structure

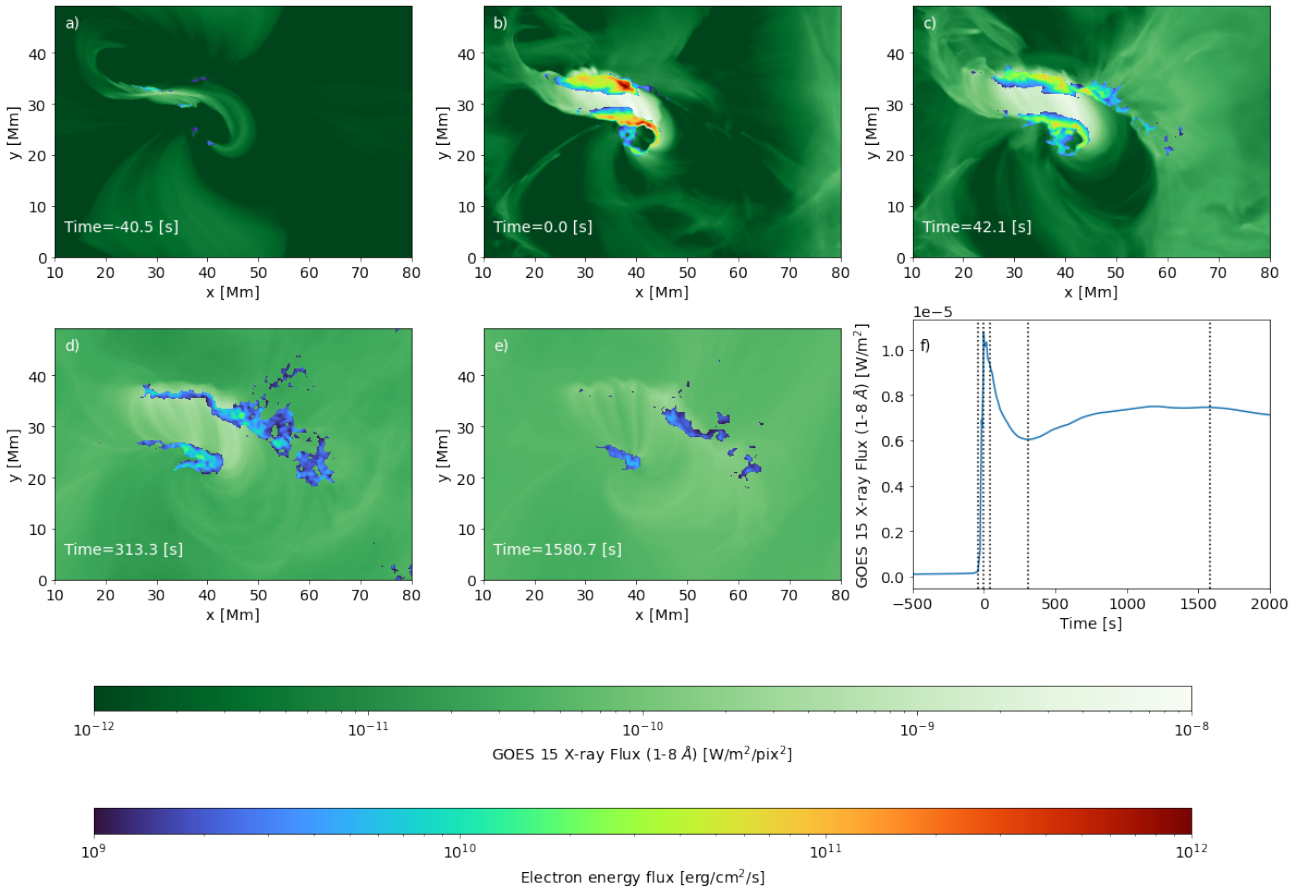

Figure 5. Evolution for flare ribbons for setup (B). In panel a)-e) we present synthetic GOES-15 soft X-ray images with an overlay of the electron energy flux at a height of 1Mm above the average $\tau = 1$ level in the simulation. Panel f) shows the integrated GOES-15 flux. Vertical dotted lines indicate the snapshots presented in panels a)-e).

in setup (A) is more arcade like (see also Fig. 9), the presence of twisted field lines suggests a hybrid state between SMA and MFR. This difference becomes evident in Figure 8, which shows the erupting MFR for both cases about 1 minute after the flare peak. The MFR in setup (B) is more strongly twisted and does carry more mass in its core. In addition to the twist number we highlight in Fig. 8 fieldlines that are connected to the reconnection region. To this end we use random seeds with a bias towards high temperature and color-code the field lines by their temperature. In both setups we find tether-cutting reconnection in a similar location. As discussed earlier, the "temperature" exceeds in these setups a billion K due to the single fluid approach that cannot separate between thermal and non-thermal particles. We find energies per particle up to 0.5 MeV at the reconnection sites.

Figures 9 and 10 show cross sections for setups A and B at the positions indicated in Figure 1 by red lines in panels b) and c). We show $|\mathbf{B}|$ on the left, the fieldline curvature $\mathbf{B} \cdot \nabla B_z / \mathbf{B}^2$ in the middle and the mass density on the right. In order to delineate cool chromospheric and filament material from the hot corona we show the $T = 50,000$ K contour in red. The contour of $B_z = 0$ G is shown in orange, while white field lines indicate the field components within the y-z plane. For setup (A) the magnetic field strength is monotonically decreasing with height for the two snapshots prior to the eruption. The fieldline curvature is negative throughout, indicating the absence of dips that can hold filament mass. Nonetheless cool material is present above the PIL and as a consequence the transition region is elevated to about 6 Mm height. A flux rope, indicated by closed field lines in the y-z plane and the presence of positive fieldline curvature is only present after the flare. Since the region with positive fieldline curvature (dipped field lines) formed above the region with enhanced mass density (at a height of about $7 - 8$ Mm), the erupting MFR carries only very little mass.

The situation is very different for setup (B), shown in Figure 10. Here a MFR with dipped field lines (positive curvature) is already present more than half an hour before the flare. The reconnection forming this MFR happens

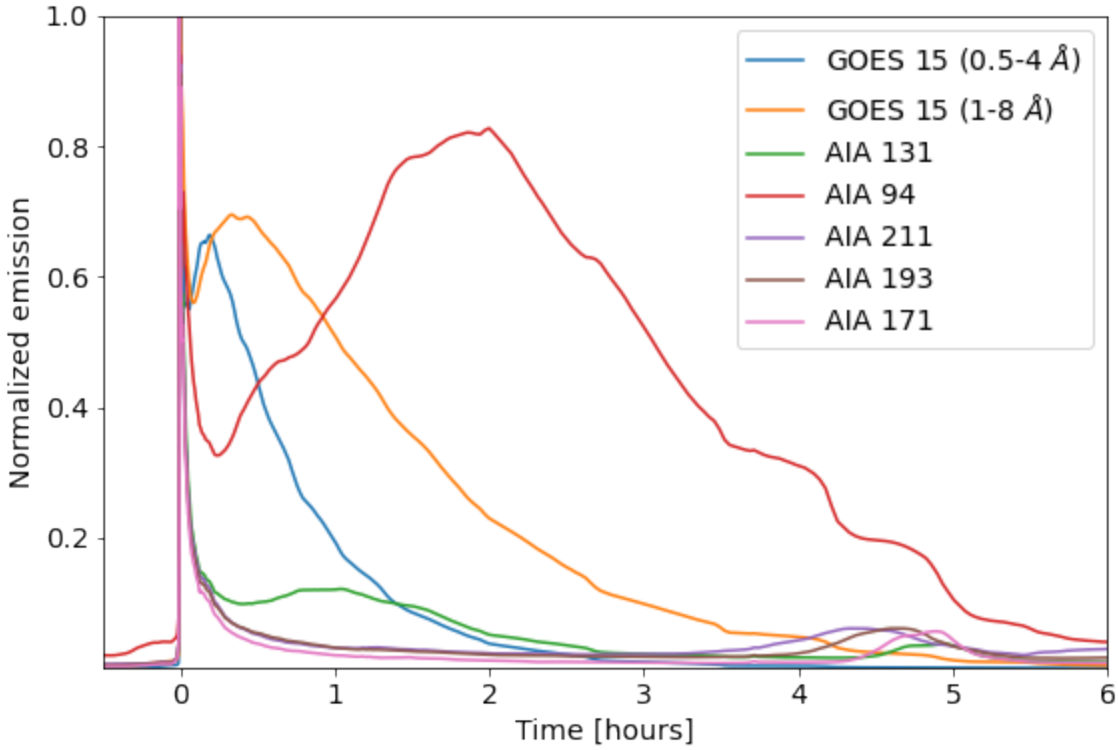

Figure 6. Post-flare evolution of GOES-15 X-ray and AIA EUV flux for setup (B). The secondary peak is present in both X-ray and EUV flux and the time-delays are consistent with a typical cooling sequence.

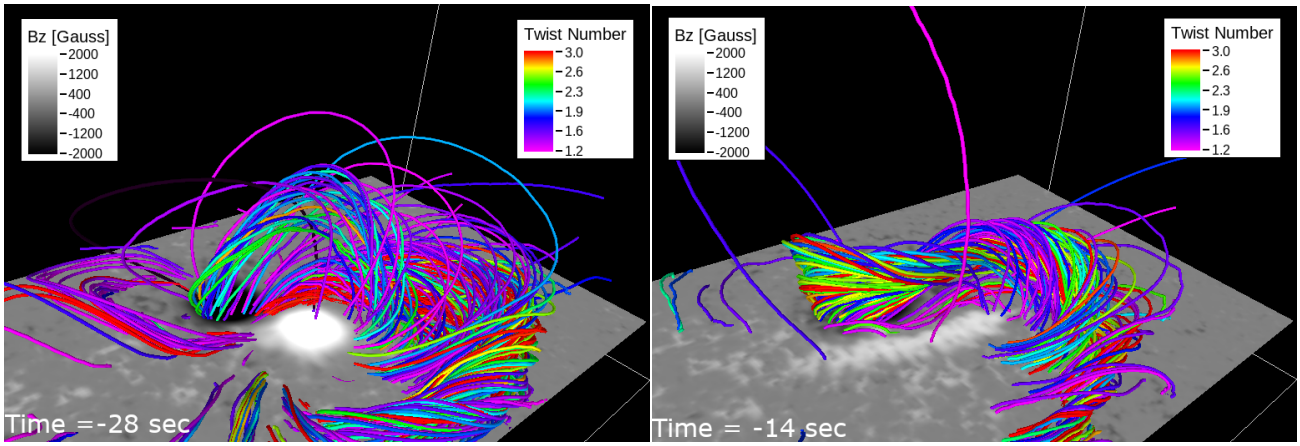

Figure 7. Pre-eruptive magnetic field configuration for the times indicated in Figure 2a) for setup (A) (left) and setup (B) (right). Magnetic field lines are color-coded according to their twist number, only field lines with values larger than 1.2 are shown. The magnetogram shows the vertical component of the the magnetic field at the average position of the photosphere. Imagery produced by VAPOR (www.vapor.ucar.edu). Animations are provided in the online material.

deep in the atmosphere close to photospheric heights and therefore results in a larger amount of filament mass supported by dipped field lines. As a consequence of the close to force-free field configuration ($(\mathbf{B}\cdot\nabla)\mathbf{B} = \frac{1}{2}\nabla\mathbf{B}^2$) the magnetic field strength has a local maximum on the MFR axis and consequently the magnetic field strength (left panels) shows little variation with height above the PIL, which is a prominent difference to setup (A) with a monotonically decreasing

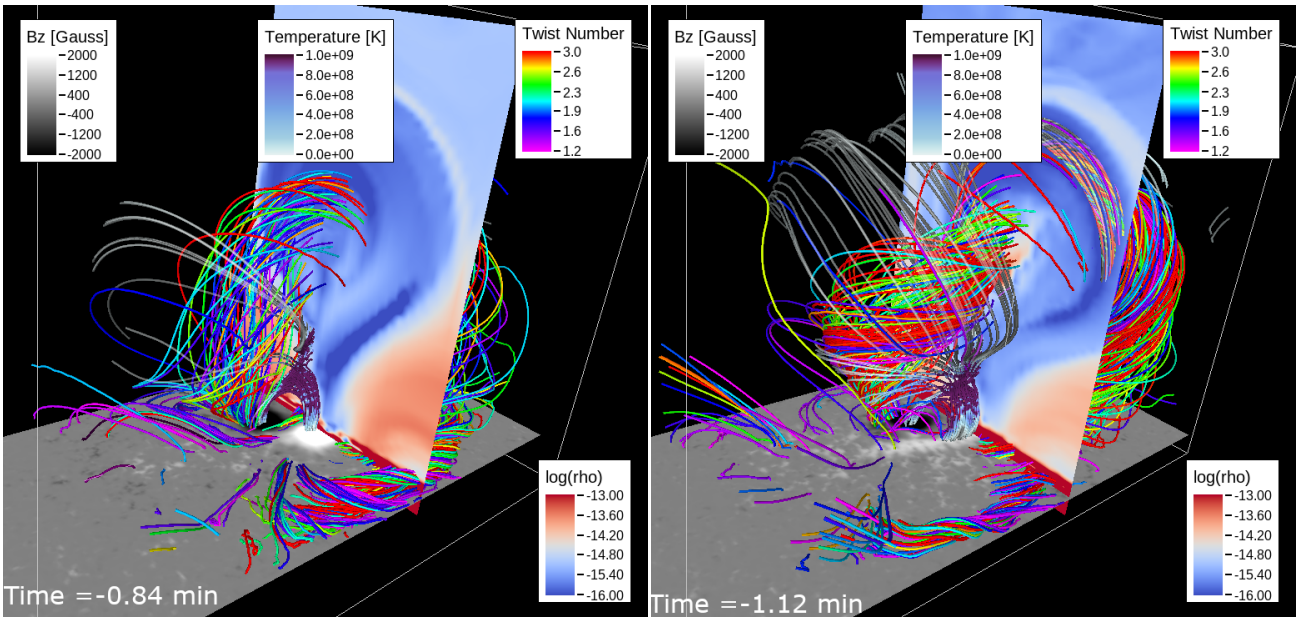

Figure 8. Magnetic field configuration about 1 minute after the flares a) for setup (A) (left) and setup (B) (right). Fieldlines are color-coded by twist number as in Figure 7. In addition we show a second set of field lines which are selected based on their connectivity to the reconnection region, these field lines are color-coded by temperature. In both setups we find tether-cutting reconnection underneath the ejected flux-ropes. We show cross-sections through the erupting flux-ropes that display the mass density. Imagery produced by VAPOR (www.vapor.ucar.edu)

field strength. About 10 minutes prior to the flare the axis of the MFR starts to rise and most of the cool material present above the PIL is lifted since it is supported by the dipped field lines. After the flare the erupting MFR carries most of the filament mass.

4. FUTURE OBSERVATIONS NEEDED TO CONSTRAIN THE PRE-ERUPTION MAGNETIC FIELD CONFIGURATION

The differences between SMA and MFR (and any transitional hybrid state) are evident at chromospheric heights since in both cases cool plasma is present to a height of about 6 Mm prior to the eruption. The most striking difference is visible in the variation of $|\mathbf{B}|$ with height, which is in the case of the SMA dropping from about 2 kG in the photosphere to less than 1 kG in a height of 5 Mm, while in the case of the MFR the field strength stays around 750 G over the same height range. While the field strength is certainly setup dependent, the presence or absence of a monotonic vertical gradient is the critical distinction between SMA and MFR as it is strongly linked to fieldline curvature. This difference is measurable with spectro-polarimetric chromospheric observations that do have a dense height coverage from photosphere to transition region. Recently, Judge et al. (2021) identified the near-UV spectral region near the Mg II lines as suitable for this. The Mg II diagnostics in the upper chromosphere can be complemented by a multitude of Fe I and Fe II lines that provide the height coverage. We note that for the distinction between SMA and MFR it is sufficient to analyze the variation of $|\mathbf{B}|$ with optical depth, a reconstruction on a physical height scale is, while certainly desirable, not strictly necessary since the difference between SMA and MFR is very striking. We strongly encourage the development of an instrument that can diagnose chromospheric magnetic field in active regions with dense height and continuous time coverage to capture the full evolution of cPILs.

5. CONCLUSIONS

Collisional shearing (Chintzoglou et al. 2019) is common in complex flare productive ARs (see, also Liu et al. 2019, 2021; Wang et al. 2022). We studied a simplified setup that only considers the interaction of 2 opposite polarities. While this setup neglects the typically more complex quadrupolar magnetic field configuration present in observed ARs, it does capture processes that happen near cPILs. Furthermore, this setup removes complexities originating from flux emergence, as we simply translate the magnetic polarities, while still enabling cancellation in the photosphere. ARs with collisional shearing do often show a deformation of colliding spots that supports the formation of a longer

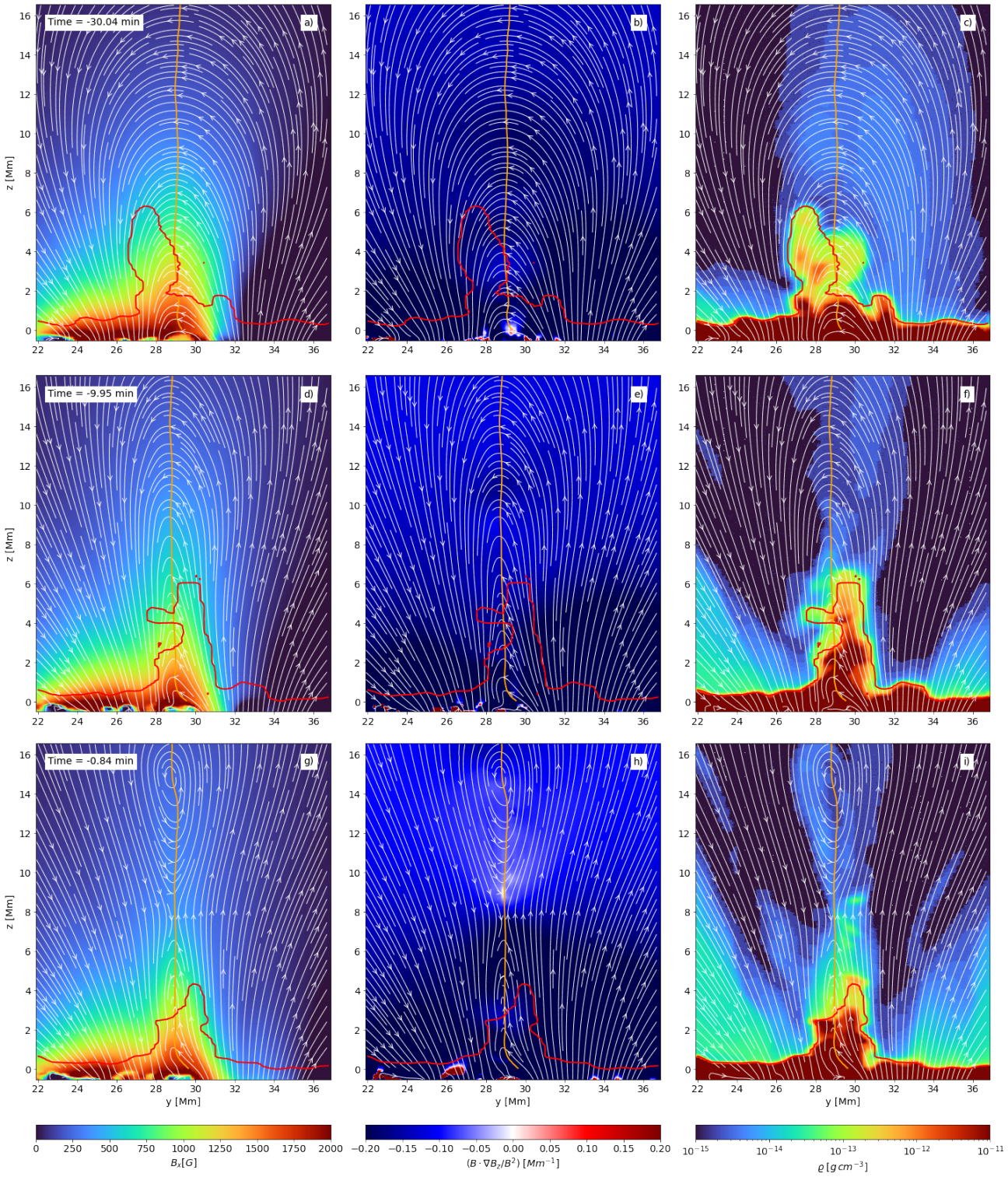

Figure 9. Cross section from Setup (A) along the cut indicated in Figure 1b). Left panels show the field strength, middle panels the fieldline curvature and right panels the mass density. Top to bottom we show the time evolution as indicated. The red line indicates the $T = 50,000$ K contour, the orange line the $B_z = 0$ contour. Fieldlines of the magnetic field within the y-z plane are shown in white. A MFR carrying very little mass is formed mostly after the eruption.

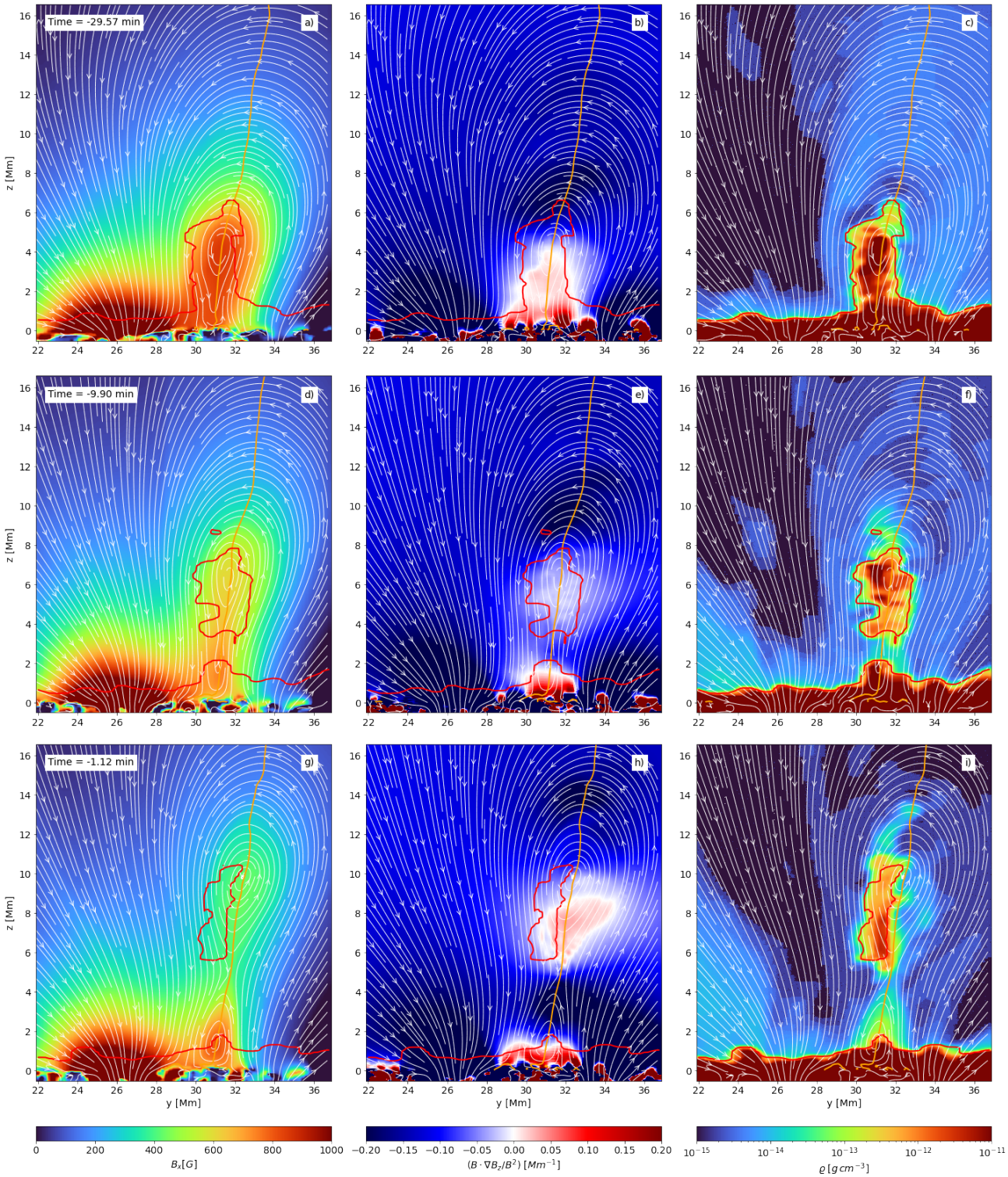

Figure 10. Cross section from Setup (B) along the cut indicated in Figure 1c). All quantities shown are as in Figure 9. Note the the different range for the field strength. A MFR is present already before the eruption and carries most of the filament mass away after the eruption.

cPIL (e.g., Chintzoglou et al. 2019). While we were able to partially emulate that effect in our setup (B) by allowing the moving spot to disperse, this is different from most observed behavior. Our spot dispersion is essentially spreading out the spot by leaving flux behind, while it would be more realistic if these fragments continue to move and through that enhance the shearing and increase the energy input into the corona.

We studied the dependence on collision distance, collision speed and spot coherence and found:

1. The collision distance is the most critical parameter influencing the strength of the resulting flare(s). Only for the 2 closest collision settings we find flares, in the more distant collision setup we find still a significant (about 2x lower) energy release in form of enhanced heating distributed over multiple hours. This is consistent with the idea of collisional shearing; a very small collision distance was associated with sunspot deformation (Chintzoglou et al. 2019).

2. Reducing the collision speed reduces the flare strength.

3. The coherence of the sunspots during the collision and therefore the length of the resulting cPIL influences critically the pre-flare magnetic field configuration, specifically whether the transition from SMA to MFR happens before or during the flare.

4. We find a similar flare energy release for both SMA and MFR setups, the primary difference is in the amount of mass that is ejected in the resulting CME (larger with pre-existing MFR).

5. The resulting lower M-class flares reach high energy densities of up to 0.5 MeV per particle and electron energy flux in excess of 10^{12} erg cm^{-2} s^{-1}. Since the resulting hot corona takes several hours to cool, they produce late-phase EUV emission.

6. Overall we find the flares resulting from collisional Polarity Inversion Lines (cPILs) very efficient, up to $40-50\%$ of the stored free energy is released in the setups with close encounter (A, B, C).

7. Spectro-polarimetric observations in the chromosphere that provide continuous height coverage from photosphere to upper chromosphere could provide direct measurements of magnetic field that allow to distinguish between SMAs and MFRs prior to eruption.

Our findings support that collisional shearing is a process that is effective in creating energetic eruptions. While our setup did not produce X-flares, it does produce significantly more energetic eruptions (up to a M1 flare) than the setup in Cheung et al. (2019) that simulated a flare arising from parasitic flux emergence. While our simulation domain and AR size (magnetic flux of 3×10^{21} Mx) are similar to Cheung et al. (2019), our most energetic flares in setups (A) and (B) release 5 times more energy (2.5×10^{31} ergs vs 5×10^{30} ergs), resulting in coronal energy densities and electron energy fluxes to the flare ribbons about an order of magnitude larger. If we extrapolate our setup to AR11158 (the colliding polarities had magnetic fluxes of $6-8\times10^{21}$ Mx (Chintzoglou et al. 2019)), we would expect that an energy release exceeding 10^{32} ergs is feasible. We find electron fluxes in excess of 10^{12} ergs cm^{-2} s^{-1}, which are towards the upper end of fluxes typically needed to explain flare ribbon properties in solar flares (Kowalski et al. 2017, 2022). The high fluxes and energy densities are a consequence of having a rather confined flaring volume in this setup, which is also the cause for late-phase EUV emission as described in Woods et al. (2011). Owing to the high temperatures reached in the flaring corona, it takes the plasma a time span of several hours to cool back to typical coronal temperatures. Synthesizing several AIA channels we find EUV flux enhancements several hours after the flare corresponding to progressing cooling sequence.

M.R. and G.C. are partially funded through NASA award 80NSSC19K0855 "Investigating the Physical Processes Leading to Major Solar Activity". Computing time was provided through NASA HECC resources under compute project s2169. L.K. is supported by a SNSF PRIMA grant. This material is based upon work supported by the National Center for Atmospheric Research, which is a major facility sponsored by the National Science Foundation under Cooperative Agreement No. 1852977. We would like to acknowledge high-performance computing support from Cheyenne (doi:10.5065/D6RX99HX) provided by NCAR's Computational and Information Systems Laboratory, sponsored by the National Science Foundation. VAPOR is a product of the National Center for Atmospheric Research's Computational and Information Systems Lab. Support for VAPOR is provided by the U.S. National Science Foundation (grants 03-25934 and 09-06379, ACI-14-40412), and by the Korea Institute of Science and Technology Information. M.R. is grateful to Stanislaw Jaroszynski and John Clyne who implemented custom changes that enable twist number calculation within VAPOR.

REFERENCES

Antiochos, S. K., DeVore, C. R., & Klimchuk, J. A. 1999, ApJ, 510, 485, doi: 10.1086/306563

Barnes, G., Leka, K. D., Schumer, E. A., & Della-Rose, D. J. 2007, Space Weather, 5, S09002, doi: 10.1029/2007SW000317

Cheung, M. C. M., Rempel, M., Chintzoglou, G., et al. 2019, Nature Astronomy, 3, 160, doi: 10.1038/s41550-018-0629-3

Chintzoglou, G., Zhang, J., Cheung, M. C. M., & Kazachenko, M. 2019, ApJ, 871, 67, doi: 10.3847/1538-4357/aaef30

Cui, Y., Li, R., Wang, H., & He, H. 2007, SoPh, 242, 1, doi: 10.1007/s11207-007-0369-5

Cui, Y., Li, R., Zhang, L., He, Y., & Wang, H. 2006, SoPh, 237, 45, doi: 10.1007/s11207-006-0077-6

Fang, F., & Fan, Y. 2015, ApJ, 806, 79, doi: 10.1088/0004-637X/806/1/79

Fisher, G. H., Canfield, R. C., & McClymont, A. N. 1985, ApJ, 289, 414, doi: 10.1086/162901

Gallagher, P. T., Moon, Y. J., & Wang, H. 2002, SoPh, 209, 171, doi: 10.1023/A:1020950221179

Georgoulis, M. K., & Rust, D. M. 2007, ApJL, 661, L109, doi: 10.1086/518718

Judge, P., Rempel, M., Ezzeddine, R., et al. 2021, ApJ, 917, 27, doi: 10.3847/1538-4357/ac081f

Kliem, B., & Török, T. 2006, PhRvL, 96, 255002, doi: 10.1103/PhysRevLett.96.255002

Kowalski, A. F., Allred, J. C., Carlsson, M., et al. 2022, ApJ, 928, 190, doi: 10.3847/1538-4357/ac5174

Kowalski, A. F., Allred, J. C., Daw, A., Cauzzi, G., & Carlsson, M. 2017, ApJ, 836, 12, doi: 10.3847/1538-4357/836/1/12

Künzel, H. 1960, Astronomische Nachrichten, 285, 271, doi: 10.1002/asna.19592850516

Linton, M. G., Dahlburg, R. B., Fisher, G. H., & Longcope, D. W. 1998, ApJ, 507, 404, doi: 10.1086/306299

Linton, M. G., Fisher, G. H., Dahlburg, R. B., & Fan, Y. 1999, ApJ, 522, 1190, doi: 10.1086/307678

Liu, L., Cheng, X., Wang, Y., & Zhou, Z. 2019, ApJ, 884, 45, doi: 10.3847/1538-4357/ab3c6c

Liu, L., Wang, Y., Zhou, Z., & Cui, J. 2021, ApJ, 909, 142, doi: 10.3847/1538-4357/abde37

Lynch, B. J., Antiochos, S. K., DeVore, C. R., Luhmann, J. G., & Zurbuchen, T. H. 2008, ApJ, 683, 1192, doi: 10.1086/589738

Patsourakos, S., Vourlidas, A., Török, T., et al. 2020, SSRv, 216, 131, doi: 10.1007/s11214-020-00757-9

Rempel, M. 2014, ApJ, 789, 132, doi: 10.1088/0004-637X/789/2/132

—. 2017, ApJ, 834, 10, doi: 10.3847/1538-4357/834/1/10

Schrijver, C. J. 2007, ApJL, 655, L117, doi: 10.1086/511857

Takasao, S., Fan, Y., Cheung, M. C. M., & Shibata, K. 2015, ApJ, 813, 112, doi: 10.1088/0004-637X/813/2/112

Toriumi, S., Iida, Y., Kusano, K., Bamba, Y., & Imada, S. 2014, SoPh, 289, 3351, doi: 10.1007/s11207-014-0502-1

Toriumi, S., & Takasao, S. 2017, ApJ, 850, 39, doi: 10.3847/1538-4357/aa95c2

van Ballegooijen, A. A., & Martens, P. C. H. 1989, ApJ, 343, 971, doi: 10.1086/167766

Wang, R., Liu, Y. D., Yang, S., & Hu, H. 2022, ApJ, 925, 202, doi: 10.3847/1538-4357/ac3f35

Woods, T. N., Hock, R., Eparvier, F., et al. 2011, ApJ, 739, 59, doi: 10.1088/0004-637X/739/2/59